CrossMark

Preparation and characterization of Eu-doped SnO_2 nanostructures for hydrogen gas sensing

Gurpreet Singh[1] · Nipin Kohli[1] · Ravi Chand Singh[1]

Abstract This paper presents effect of europium doping on the structural, optical and gas sensing properties of SnO_2 nanoparticles. XRD (X-ray diffraction) and Raman results confirmed tetragonal rutile structure of both undoped as well as Eu-doped SnO_2 nanoparticles. The crystallite size has decreased systematically with increase in dopant concentration as confirmed from XRD and TEM (Transmission electron microscopy) investigations. The shifting and broadening of Raman bands has been explained on the basis of phonon confinement effect. Raman spectra exhibited bands centered at 567 and 523 cm^{-1} which are associated with the Raman surface modes and whose contribution has been found to increase with increase in the dopant concentration. The intensity of emission peaks in the PL (Photoluminescence) spectra has been found to decrease with increase in dopant concentration which can be attributed to the concentration quenching effect. The operating temperature of all the sensors has been investigated which optimized at 350 °C. There has been a significant enhancement in sensor response towards hydrogen due to Eu doping which optimized at 3 % dopant concentration.

1 Introduction

Hydrogen is a green fuel and has extensive utility in rocket engines, power generation, transportation and industrial use. It is colourless, odourless, explosive and extremely inflammable in the concentration range of 4–74 % [1]. Therefore, imperatively highly sensitive hydrogen sensors are needed to be developed for an early detection and leakage warning system. It is well known fact that SnO_2 exhibits insulating character in its stoichiometric form whereas nonstoichiometry, such as oxygen vacancies, induces conducting behavior [2]. It is noteworthy that SnO_2 is an n-type wide band semiconductor which finds applications in fabricating solar cells, lithium batteries, transparent conductive electrodes etc. [3–5]. In addition to the above applications, SnO_2 has been largely investigated as a gas sensing material due to its low cost, high sensitivity, simple synthesis procedure and high thermal and chemical stability [6].

The gas sensing mechanism involves reaction between adsorbed oxygen species and test gas molecules on the surface of sensing material. When SnO_2 is placed in air ambience, oxygen gets adsorbed on its surface capturing electron from the conduction band which results in formation of ionic species such as O_2^-, O^- and O^{2-} depending upon the operating temperature. The reaction between adsorbed oxygen and reducing gas at the surface injects electron back into conduction band leading to decrease in electrical resistance of n-type SnO_2 [7]. The concentration of adsorbed oxygen depends mainly upon surface area and surface morphology of material used [8].

It has been reported that the gas sensing properties of SnO_2 can be improved by employing different methods such as morphology modification of nanostructures, surface area enhancement, adding catalysts, dopants etc. [9–12]. Nanostructured materials have been regarded as the best candidates for improving the gas sensitivity significantly owing to their small particle size and large surface to volume ratio. Xu et al. [13] studied the effect of grain size

✉ Ravi Chand Singh
  ravichand.singh@gmail.com

[1] Department of Physics, Guru Nanak Dev University, Amritsar 143005, India

on the sensor response of SnO_2 and observed that when the size of SnO_2 was reduced to below 10 nm, there was remarkable increase in sensor response towards hydrogen gas. Kida et al. [14] studied the effect of pore and particle size on the hydrogen gas sensing properties of SnO_2 nanoparticles. The large surface area of metal oxide nanostructures offers huge number of active sites for gas adsorption which leads to enhancement in sensing response.

Earlier studies suggested that doping is very effective method for improving the gas sensing properties of SnO_2 based nanostructures [15]. In addition to electronic properties, doping also modifies the structural properties of grains such as size and shape. Lately, among various choices of dopants rare earths have gained much attention for improving gas sensing because rare earth oxides provide high surface basicity, fast oxygen ion mobility and excellent catalytic properties which are important features for chemical sensing [16].

In the present study, we report the role of europium doping on the gas sensing properties of SnO_2 nanoparticles. Though a significant number of articles are available on improvement of hydrogen sensitivity using Pd/Pt catalyst [17–19] but to the best of our knowledge there are no reports on selective enhancement of hydrogen sensing employing Eu as a dopant in SnO_2 nanostructures. Our results indicated that sensor response towards hydrogen gas became rapid and optimally enhanced at 3 % doping of Eu into SnO_2. Experimental data revealed that crystallite size has been decreased, which ultimately increased the surface area, with increase in dopant concentration. The enhanced sensor response has been attributed to the increased surface area of doped nanoparticles. Moreover, it has also been observed that Raman surface modes are directly linked with surface area of nanoparticles.

2 Experimental

All chemical used in the present study were of analytical grade. $SnCl_4 \cdot 5H_2O$ and Eu $(NO_3)_3 \cdot 5H_2O$ were purchased from Sigma Aldrich whereas ammonium hydroxide was acquired from Loba Chemie.

Undoped and Eu-doped SnO_2 nanoparticles were prepared by chemical co-precipitation method. Initially, 0.1 M aqueous solution of $SnCl_4 \cdot 5H_2O$ was prepared to which ammonium hydroxide solution was added drop wise with continuous stirring until the pH of solution reached at 9. This process led to formation of white precipitates which were filtered, washed and dried into powder form and calcined at 500 °C. Eu-doped samples (with 1–5 % content) were prepared by above mentioned procedure by adding Eu $(NO_3)_3 \cdot 5H_2O$ into $SnCl_4 \cdot 5H_2O$ solution.

The crystal structure of undoped and Eu-doped SnO_2 nanoparticles has been studied by using Shimadzu 7000 Diffractometer system with Cu Kα radiation in the scanning range varying from 20° to 80°. The specific surface area has been determined by single point Brunauer Emmett Teller (BET) surface area analyzer (Micromeritics ASAP 2020). Raman spectra of all the samples were recorded using Renishaw InVia Micro Raman spectrometer with excitation wavelength 514 nm. Photoluminescence studies have been performed with the help of Perkin Elmer LS55 fluorescence spectrometer. TEM micrographs of nanoparticles were obtained using JEOL JEM-2100 operating at 200 keV.

2.1 Fabrication of thick film sensor and testing system

The suitable amount of powder sample was mixed with few drops of distilled water to make a paste. After that with the help of fine brush the paste was painted on to the alumina substrate to form a thick film between two gold electrodes. For the deposition of gold electrodes liquid bright gold paint (purchased from Hobby Colorobbia Bright Gold) was painted on alumina substrate leaving 2 mm gap between two electrodes. Finally the alumina substrate was heat treated to convert paint into metallic gold. The procedure mentioned above was adopted for the fabrication of doped sensors with different europium contents. The thick film sensors with gold electrodes were heated at 300 °C.

The gas sensing characteristics of fabricated sensors have been studied with the help of home assembled apparatus having 40 L test chamber consisting of small temperature controlled oven and circulating fan with simple potentiometric arrangement. The picture of actual experimental set up of gas sensor is as shown in Fig. 1a. In order to measure the sensor response the sensor under investigation was placed inside the temperature controlled oven where the temperature of thick film sensor can be varied. The schematic diagram of electric circuit of sensing unit is demonstrated in Fig. 1b. The variation of real time voltage signal as a function of time across resistance R_L connected in series with sensor resistance R_S has been recorded using data acquisition Module KUSB-3100 and computer. In order to measure the sensor response a known quantity of test gas was injected into test chamber. The current flowing through the circuit has been determined by relation V_O/R_L and the sensor resistance of undoped and Eu-doped SnO_2 sensors has been determined by using following equation:

$$V_I = I(R_S + R_L) \tag{1}$$

where R_S is the sensor resistance, R_L is the variable resistance.
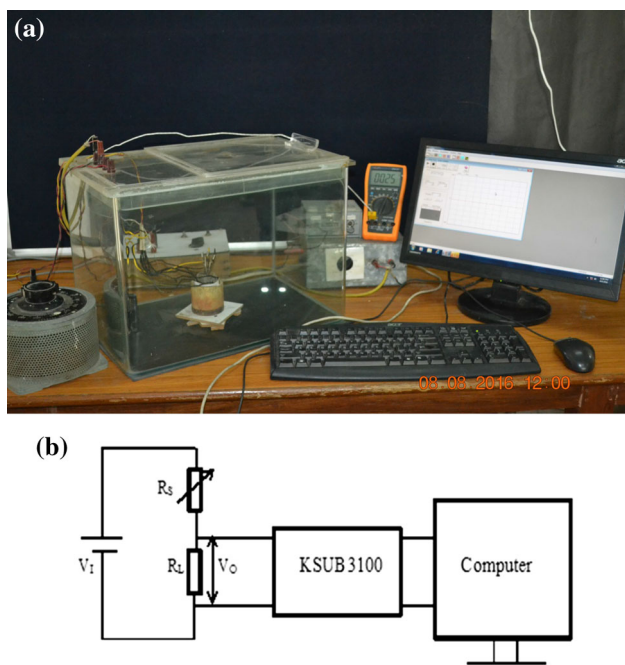
Fig. 1 **a** Diagram showing actual experimental set up of gas sensor, **b** schematic diagram showing circuit of sensing unit

Fig. 2 XRD patterns of undoped and Eu-doped SnO_2 nanoparticles

The sensor response of fabricated sensors has been determined by using following relation:

$$\text{Sensor response} = \frac{R_a}{R_g} \tag{2}$$

where R_a is the sensor resistance in the presence of air, R_g is the sensor resistance in air-gas mixtures.

3 Results and discussion

3.1 X-ray diffraction

Figure 2 represents XRD patterns of undoped and Eu-doped SnO_2 nanoparticles. The indexing of XRD peaks of undoped and Eu-doped nanoparticles has been achieved by using JCPDS data. The crystal structure of all the samples was found to be rutile type tetragonal structure. The crystallite size has been calculated by Scherrer's formula given by [20]:

$$D = \frac{K\lambda}{\beta \cos \theta} \tag{3}$$

where λ is the wavelength of incident X-rays, β is the full width at half maximum (FWHM) of XRD peaks, θ is the Bragg's angle.

The absence of peaks related to europium oxide in doped samples confirmed that dopant has been incorporated into lattice sites of SnO_2. The experimental data revealed that the crystallite size (Table 1) decreased with
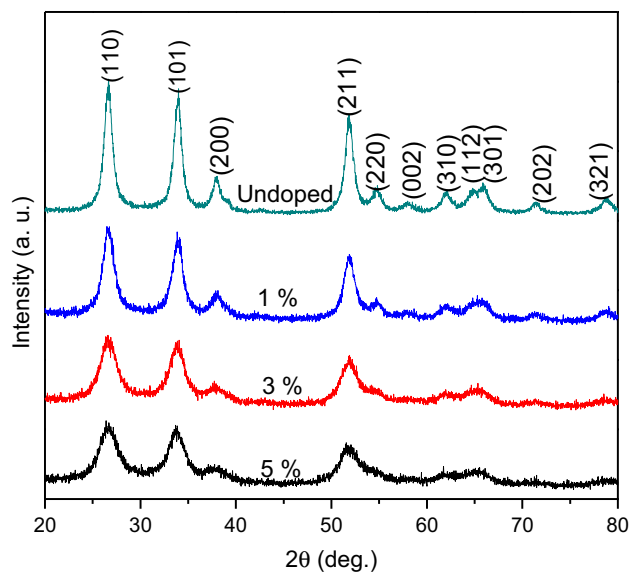
increase in dopant concentration which implies that dopant inhibited the growth of SnO_2 during synthesis process. Furthermore, the decrease in intensity of XRD peaks with increase in dopant concentration indicates decrease in crystallinity of doped nanoparticles.

3.1.1 Estimation of lattice strain: Williamson-Hall analysis

XRD peak broadening is mainly caused by two factors (1) particle size, and (2) lattice strain. Scherrer's formula does not take care of lattice strain whereas Williamson-Hall method (WH-analysis) does consider lattice strain. The strain present in the samples is given by:

$$\varepsilon = \frac{\beta_{hkl}}{4 \tan \theta} \tag{4}$$

W–H method of analysis calculates the lattice strain as well as crystallite size of nanoparticles. Since two factors (particle size and strain) contribute to the peak broadening, therefore a peak can be represented by sum of two contributions: i.e. crystallite size and lattice strain [21]:

$$\beta_{hkl} = \frac{K\lambda}{D \cos \theta} + 4\varepsilon \tan \theta \tag{5}$$

The rearrangement of above equation gives:

$$\beta_{hkl} \cos \theta = \frac{K\lambda}{D} + 4\varepsilon \sin \theta \tag{6}$$

where β_{hkl} is FWHM of diffraction peak, ε is the strain present in the samples.

Equations (4) and (5) are recognized as WH- equations. In order to calculate the lattice strain and crystallite size from WH-method, a graph between $\frac{\beta \cos \theta}{\lambda}$ in y-axis and $\frac{\sin \theta}{\lambda}$

Table 1 Crystallite size, lattice strain and BET surface area of undoped and Eu-doped SnO$_2$

Sample	Crystallite size using Scherrer's formula (nm)	Crystallite size from WH plot (nm)	Particle size from TEM (nm)	Lattice strain	BET surface area (m^2/g)
Undoped	8.7	8.5	9.8	−0.00737	44.80
1 %	6	5.5	–	−0.01542	49.58
3 %	4.2	4	3.98	−0.03759	58.50
5 %	3.6	2.9	–	−0.05451	87.48

in x-axis has been plotted. The slope and intercept of linear fitted plot (Fig. 3) gives magnitude of lattice strain and crystallite size respectively which have been shown in Table 1. The negative value of slope for undoped and Eu-doped SnO$_2$ implies presence of compressive strain in the lattice [22]. It can be seen from the Table 1 that compressive strain has been increased with increase in dopant concentration.

3.2 BET surface area analysis

The BET surface area was measured by nitrogen adsorption for undoped and Eu doped SnO$_2$ nanoparticles. Table 1 represents the values of BET surface area for undoped and Eu-doped SnO$_2$ nanoparticles. It is evident from the values given in Table 1 that the BET surface area has been increased with decrease in particle size.

3.3 Energy dispersive spectra (EDS)

In order to confirm the presence of Eu in the doped samples EDS spectra have been recorded which have been shown in Fig. 4a, b. The spectra of undoped sample (Fig. 4a) contain
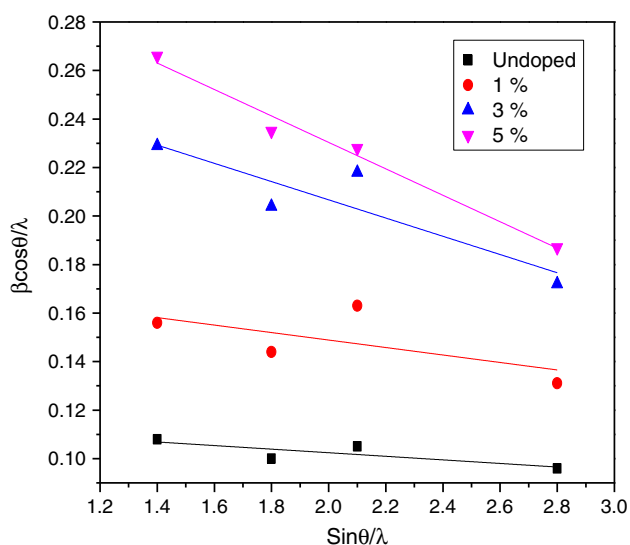
Fig. 3 Williamson-Hall plots of undoped and Eu-doped SnO$_2$ nanoparticles

peaks corresponding to Sn and O whereas spectra of 3 % doped nanoparticles (Fig. 4b) display peaks corresponding to Eu, Sn and O. The absence of other peaks confirmed purity of synthesized samples.

### 3.4 Transmission electron microscopy

Figure 5a shows the TEM image of undoped SnO$_2$ nanoparticles and Fig. 5b, c displays HRTEM images of undoped and 3 % doped SnO$_2$ nanoparticles. The particle size and interplanar spacing has been determined by using image J software. The calculated value of particle size of undoped and 3 % doped samples has been represented in Table 1 which clearly shows the reduction of particle size of 3 % doped nanoparticles as compared to undoped nanoparticles. The interplanar spacing (0.33 nm) calculated from HRTEM image of undoped nanoparticles corresponded to (110) planes of tetragonal rutile structure of SnO$_2$.

3.5 Raman spectroscopy

Raman spectroscopy is an excellent technique for probing crystal structure, defects, electronic structure and size effects in nanostructures. The unit cell of SnO$_2$ consists of two tin and four oxygen atoms producing 18 vibration modes in first brilluion zone. The normal vibration modes of SnO$_2$ at the center of brilluion zone can be represented by group theory as [23]:

$$\Gamma = A_{1g} + A_{2g} + B_{1g} + B_{2g} + E_g + 2A_{2u} + 2B_{1u} + 4E_u \tag{7}$$

Out of these 18 vibrational modes four modes are Raman active (three non-degenerate modes A_{1g}, B_{1g}, B_{2g} and a doubly degenerate mode E_g), two modes are IR active (non- degenerate A_{2u} and the triply degenerate E_u), A_{2g} and B_{1u} modes are silent. One A_{2u} and two E_u modes are acoustic. Raman active non-degenerate modes (A_{1g}, B_{2g} and B_{1g}) vibrate in the plane perpendicular to c–axis whereas vibrations of doubly degenerate modes are along the direction of c-axis. In E_g mode oxygen atoms vibrate in oxygen plane while in other two modes (A_{1g}, B_{2g}) the
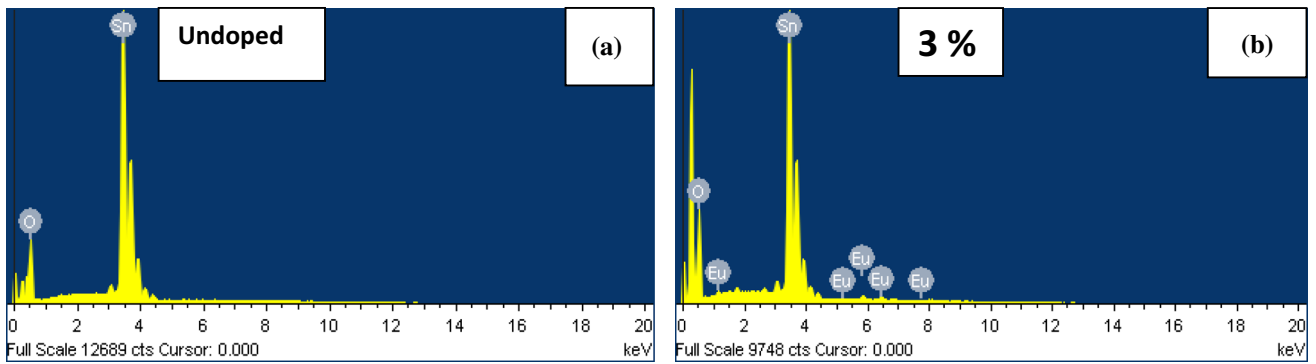
Fig. 4 EDS spectra of **a** undoped, **b** 3 % Eu-doped SnO$_2$ nanoparticles
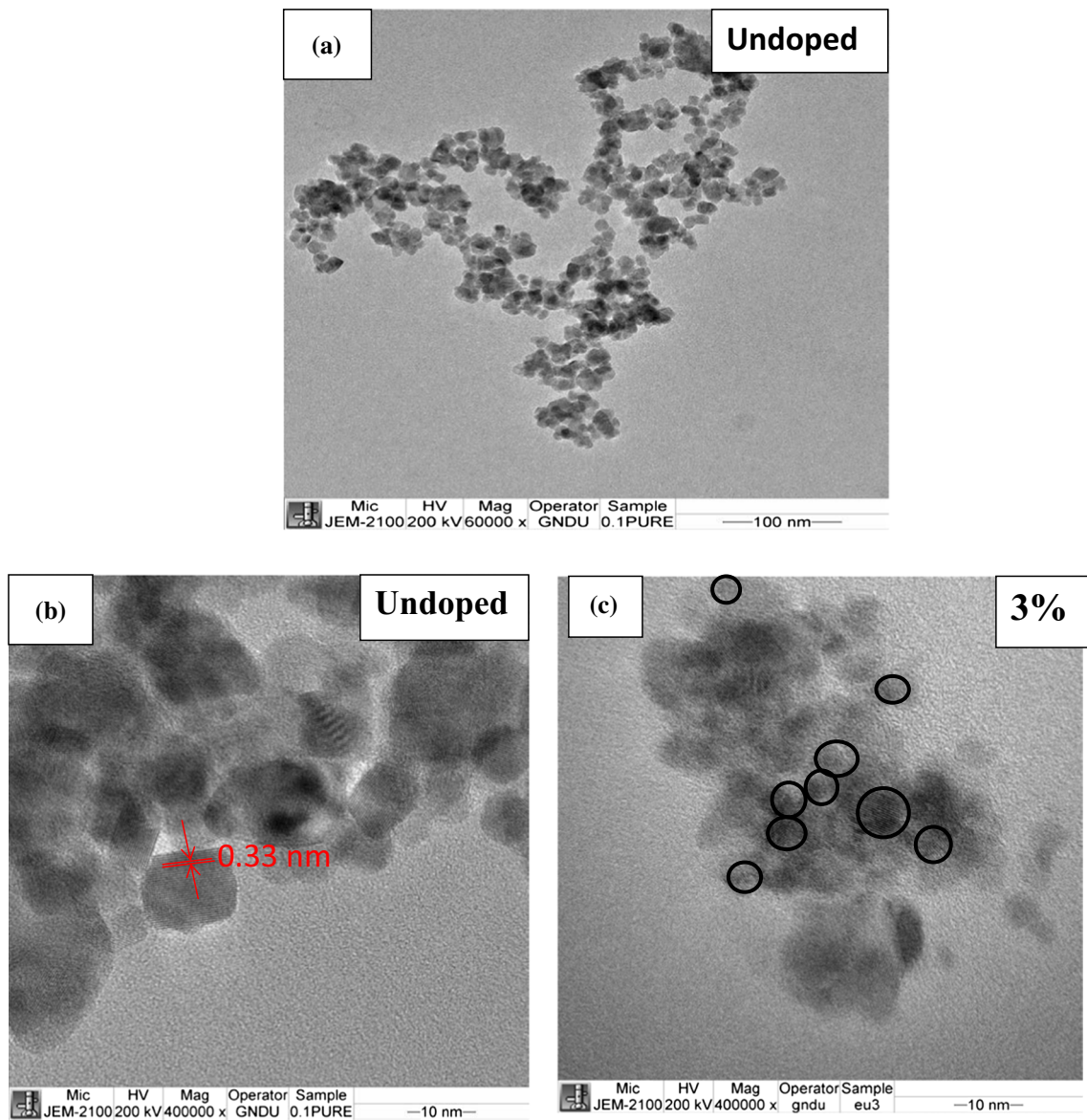
Fig. 5 TEM image of **a** undoped nanoparticles, HRTEM images of **b** undoped, **c** 3 % doped SnO$_2$ nanoparticles
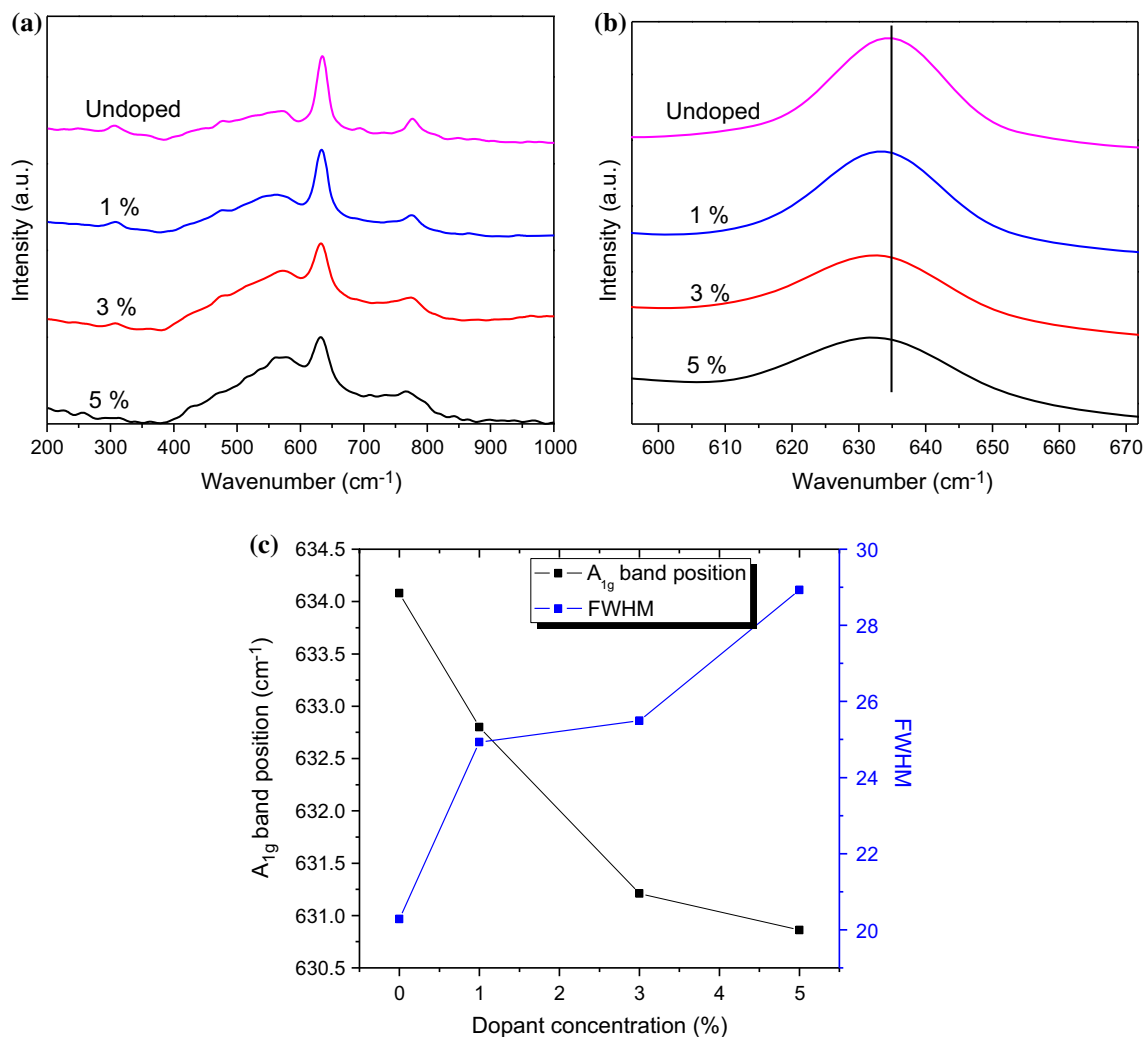
Fig. 6 **a** Room temperature Raman spectra of undoped and Eu-doped SnO$_2$ nanoparticles, **b** diagram showing shifting of A$_{1g}$ band as a function of dopant concentration, **c** variation of peak position and FWHM of A$_{1g}$ band as a function of dopant concentration

expansion and contraction of Sn–O bonds takes place. Figure 6a depicts room temperature Raman spectra of undoped and Eu-doped SnO$_2$ nanoparticles which exhibit bands positioned at 475, 634.4 and 775 cm^{-1} associated with E$_g$, A$_{1g}$ and B$_{2g}$ fundamentals modes of tetragonal rutile SnO$_2$ respectively [24]. Appearance of bands centered at 306 cm^{-1} is attributed to the formation of SnO$_2$ particles in nano regime [25]. It is quite clear from Fig. 6b that A$_{1g}$ band becomes broad and shifts towards lower wavenumber with increase in dopant concentration. The variation of peak position and FWHM of A$_{1g}$ band with increase in dopant concentration is represented in Fig. 6c. Such a shifting and broadening of A$_{1g}$ band has been ascribed to the confinement of optical phonons in small crystals. As the particle size is reduced to the order of few nanometers, the wave function of optical phonons is not associated with plane wave but it becomes localized which leads to breakdown of selection rule of wave vector

conservation. Therefore, phonons with zero wave vector q = 0 along with phonons with q > 0 contributes to Raman scattering which results in shifting and broadening of Raman bands [26, 27].

As revealed from Fig. 6a Raman spectra of undoped and Eu-doped SnO$_2$ nanoparticles present broad features between 380 and 600 cm^{-1} called Raman surface modes. The fitting of Raman spectra assuming lorentzian shaped peaks revealed additional bands positioned at 523 (S$_1$) and 567 (S$_2$) cm^{-1} which is attributed to surface phonon modes. The fitted spectra of undoped nanoparticles have been shown in Fig. 7a. These bands (S$_1$ and S$_2$) might have originated from vibrational modes of particle surface where imperfections probably modify the local symmetry giving rise to modes in addition to the bands present in the deep inside the particle core [25, 28].

In order to estimate the contribution of Raman surface modes the ratio of A$_{S1+S2}$ and A$_{1g}$ is considered where
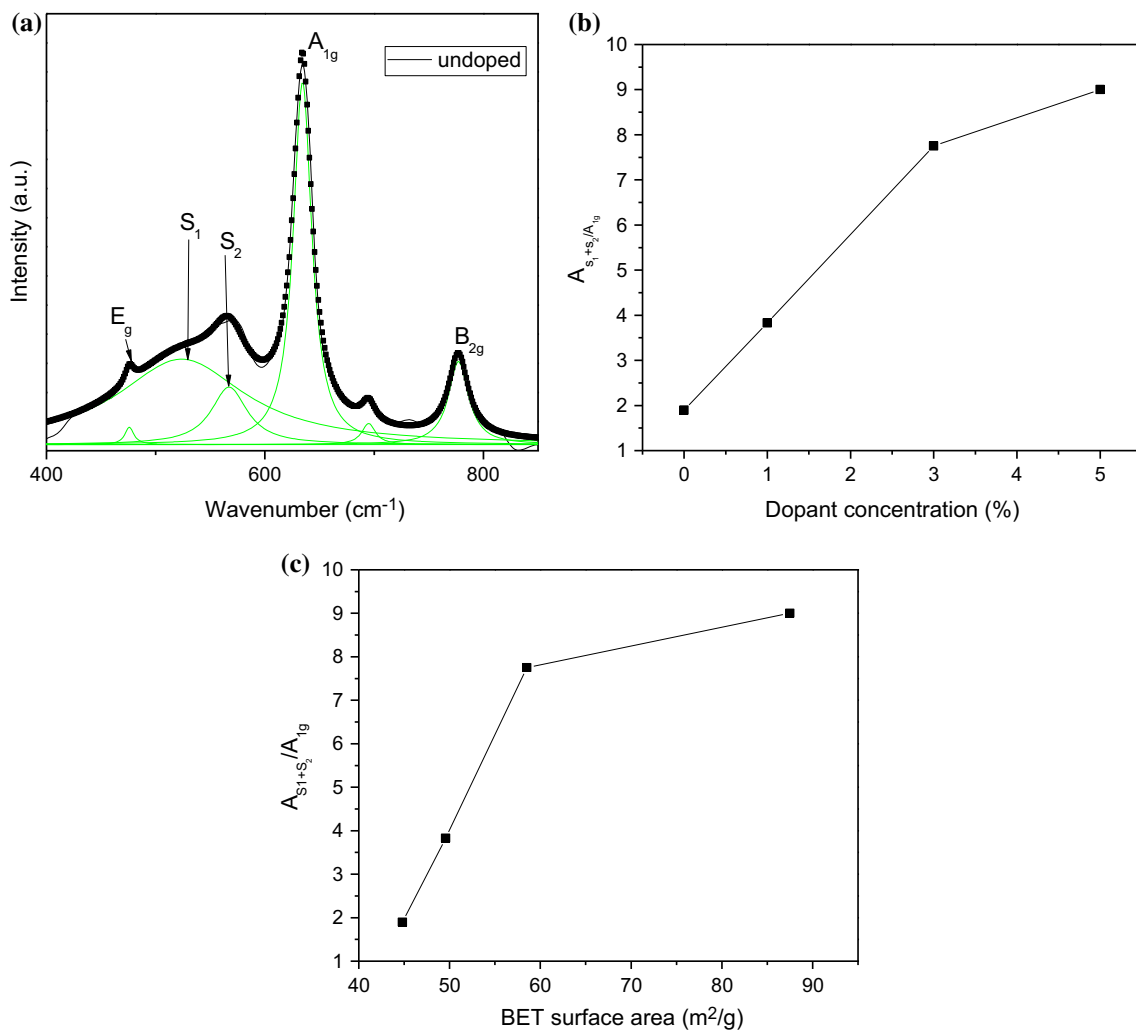
Fig. 7 a Fitted Raman spectra of undoped SnO_2 nanoparticles, b variation of surface modes as a function of dopant concentration, c variation of surface modes with surface area

A_{S1+S2} represents summed areas of surface modes and A_{1g} represents area of A_{1g} mode. Figure 7b, c display the ratio of summed area of surface bands to area of A_{1g} modes as a function of dopant concentration and surface area. The above Fig. 7b, c signified that the contribution of Raman surface modes grows with increase in dopant concentration and surface area. It has been reported that the relative intensity of Raman surface modes is related to the specific surface area of nanoparticles [29]. Therefore, our results are consistent with the previous reports.

3.6 Photoluminescence spectra

Photoluminescence spectroscopy probes structural defects and impurities in metal oxide semiconductors. Figure 8 shows the room temperature PL spectra of undoped and Eu-doped SnO_2 nanoparticles. All the samples produced emission peaks centered at 418, 441, 461, 483 and 525 nm

respectively. These emission peaks in the visible region are associated with defect energy levels originating from tin interstitials and oxygen vacancies in SnO_2 [30]. The oxygen vacancies are known as the most common defects in metal oxide semiconductors which form donor levels inside the band gap and play important role in PL process. In metal oxide semiconductors oxygen vacancies exists in different charge states such as V_O^0, V_O^+, V_O^{++}.

When V_O^0 (an oxygen vacancy without any positive charge) centers dissociate (at room temperature) they provides V_O^+ (oxygen vacancy with positive charge) centers and conduction band electrons. When UV radiation falls on the SnO_2 the electron from the valence band is excited to conduction band leaving hole in the valence band. This active hole recombines with electron in V_O^+ center which forms V_O^{++} center. The recombination of conduction band electron with V_O^{++} center gives visible emission [31]. It can be clearly seen from the Fig. 8 that the intensity of
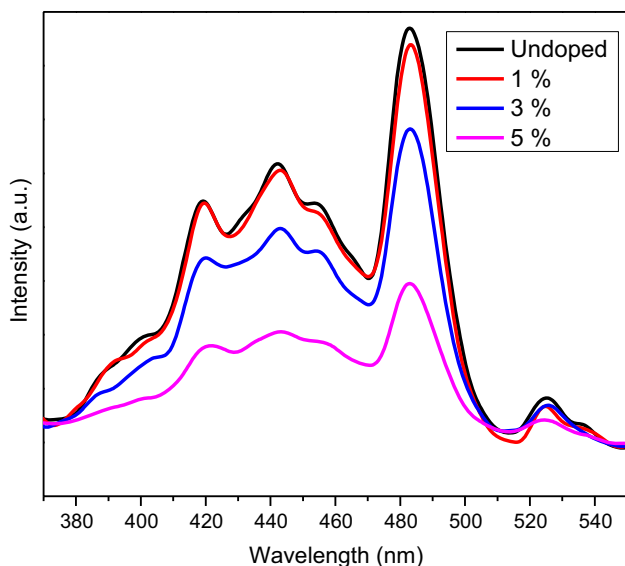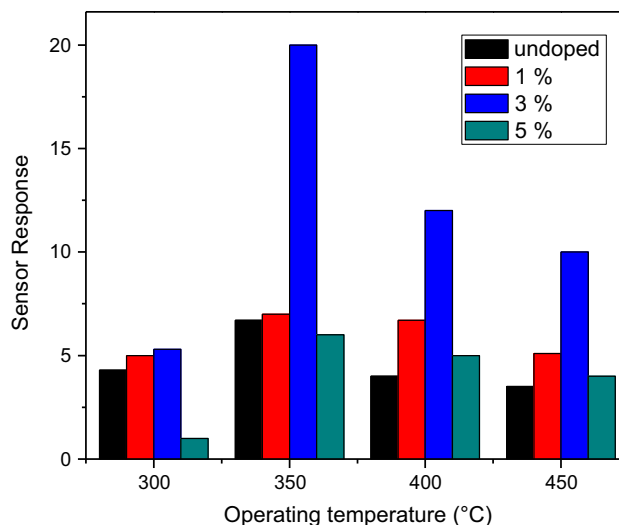
Fig. 8 Photoluminescence spectra of undoped and Eu-doped SnO$_2$ nanoparticles

Fig. 9 Sensor response of undoped and Eu-doped sensor to 300 ppm of hydrogen gas at various operating temperature

emission peaks has been decreased with increase in dopant concentration and it can be attributed to concentration quenching effect which is described by cross-relaxation process. This process involves the exchange of energy between a pair of neighboring ions and migration of excitation energy [30].

4 Gas sensing properties

4.1 Sensor response

It is well known fact that the gas sensor response is highly dependent on the operating temperature and dopant concentration. In order to determine the optimum operating temperature and optimum doping amount the sensors fabricated from powder samples were exposed to 300 ppm of hydrogen at different operating temperature (300–450 °C). Figure 9 shows the sensor response of all the samples towards 300 ppm of hydrogen gas at various operating temperatures. It has been observed that sensor response of fabricated sensors optimized at 350 °C. It is quite obvious from above Fig. 9 that the sensor response optimized at 3 % dopant concentration. Therefore, 3 % dopant concentration improved sensor response significantly as compared to undoped sensor. Figure 10 shows variation of sensor resistances of undoped and 3 % Eu doped sensor towards 300 ppm of hydrogen gas. Sensor response is obtained from sensor resistance variation in the presence of hydrogen gas as shown in Fig. 11 which exhibits response-recovery characteristics of sensor. Evidently the sensor response towards hydrogen gas can be improved
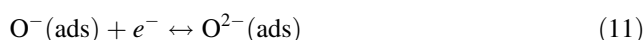
significantly after incorporation of Eu into SnO$_2$. A slight improvement in response time has been registered with doping as tabulated in Table 2.

4.2 Gas sensing mechanism

The gas sensing mechanism of SnO$_2$ involves the interaction between adsorbed oxygen on the surface and test gas. When metal oxide such as SnO$_2$ is placed in air then atmosphere oxygen is adsorbed on the surface of SnO$_2$ and adsorbed oxygen gets ionize in different forms such as O_2^-, O^- and O^{2-} by capturing electrons from the conduction band of SnO$_2$. The ionized oxygen forms electron depletion layer on the surface of n-type SnO$_2$. Therefore, the resistance of sensing material increases in the presence of air. When sensor is exposed to reducing gas, the adsorbed oxygen reacts with reducing gas and captured electron go back to conduction band [32]. Therefore the conductivity of SnO$_2$ increases when exposed to reducing gas. The reaction mechanism can be represented as:
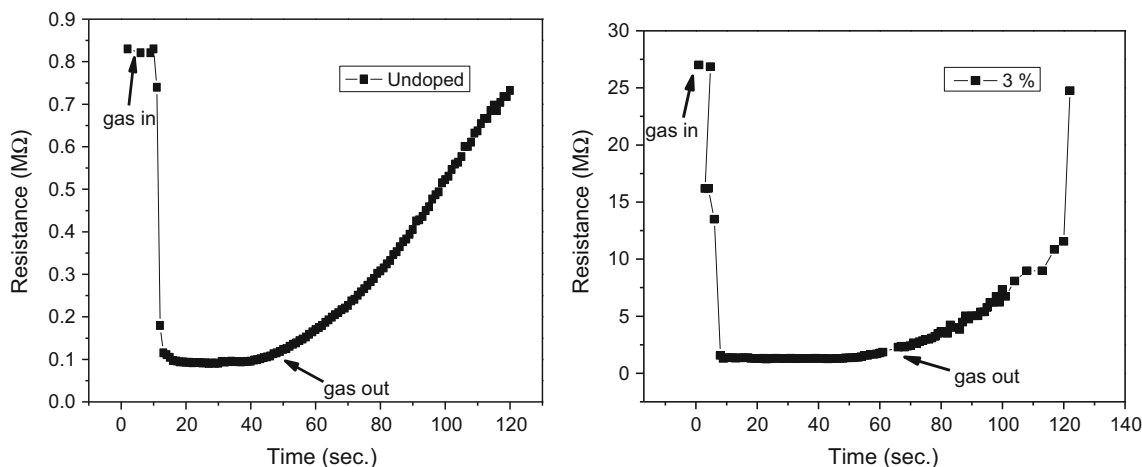
$$O_2 \text{ (air)} \leftrightarrow O_2(\text{ads}) \tag{8}$$

$$O_2(\text{ads}) + e^- \leftrightarrow O_2^-(\text{ads}) \tag{9}$$

$$O_2^-(\text{ads}) + e^- \leftrightarrow 2O^-(\text{ads}) \tag{10}$$

$$O^-(\text{ads}) + e^- \leftrightarrow O^{2-}(\text{ads}) \tag{11}$$

The reaction between oxygen species and hydrogen gas can be depicted as follows:
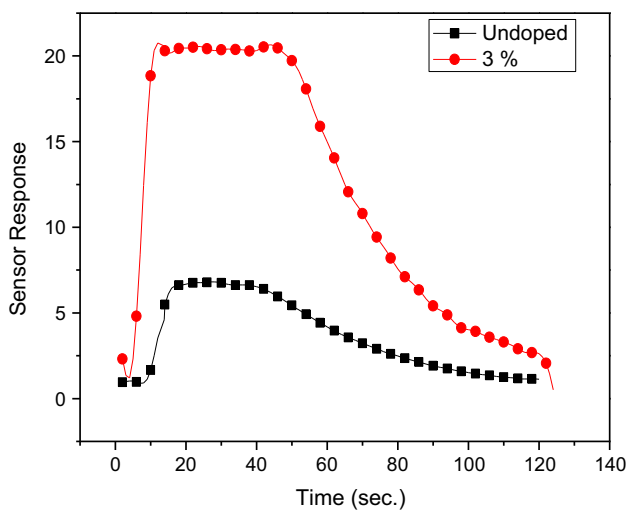
$$H_2 + O^- \rightarrow H_2O + e^- \tag{12}$$

The improved sensor response of Eu-doped SnO$_2$ sensors can be explained on the basis of following reasons:

Fig. 10 Sensor resistance variation with time for undoped and Eu-doped SnO$_2$ sensors to 300 ppm of hydrogen gas
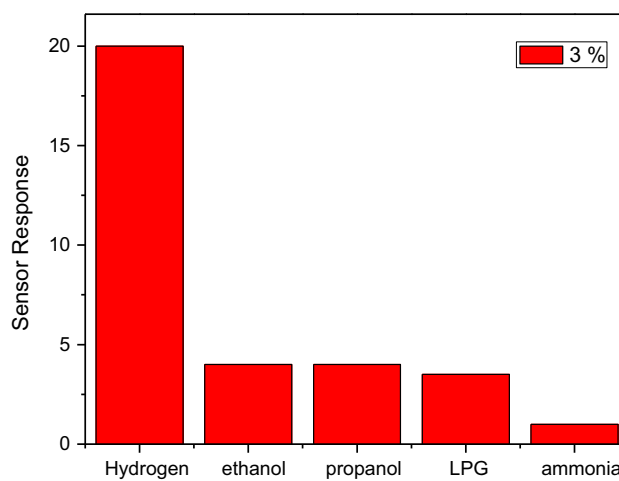

Fig. 11 Response-recovery characteristics of undoped and 3 % doped sensors at 350 °C

Fig. 12 Sensor response of 3 % doped sample to 300 ppm of hydrogen, ethanol, propanol, LPG and ammonia gas at 350 °C

Table 2 Response times of undoped and 3 % doped SnO$_2$ sensors

Sample	Response time (s)
Undoped	11
3 %	7

XRD and TEM results revealed (Table 1) that particle size has been reduced with increase in dopant concentration. Moreover, BET studies confirmed increase in surface area with decrease in particle size which leads to increase in concentration of adsorbed oxygen on the surface of doped samples thereby enhancing the sensor response towards hydrogen gas [8]. It has been reported that the Raman surface modes are related to available surface sites that interact with target gas. Rumyantseva et al. [33] showed that the sensor response towards reducing gas increases with increase in contribution of Raman surface

modes. We have observed that the contribution of Raman surface modes has been increased with dopant concentration. Therefore, we believe that improved sensor response of Eu-doped SnO$_2$ sensor towards hydrogen gas might be attributed to enhanced contribution of Raman surface modes.

4.3 Selectivity

In addition to the sensor response the selectivity of sensor is also an important parameter. In order to check the selectivity of 3 % doped sensor, it was exposed to 300 ppm of hydrogen, ethanol, propanol, LPG and ammonia as shown in Fig. 12. The results indicated that the sensor response towards hydrogen gas was significantly higher than other test gases. Interestingly, the sensor fabricated from 3 % doped SnO$_2$ showed good selectivity towards hydrogen gas.
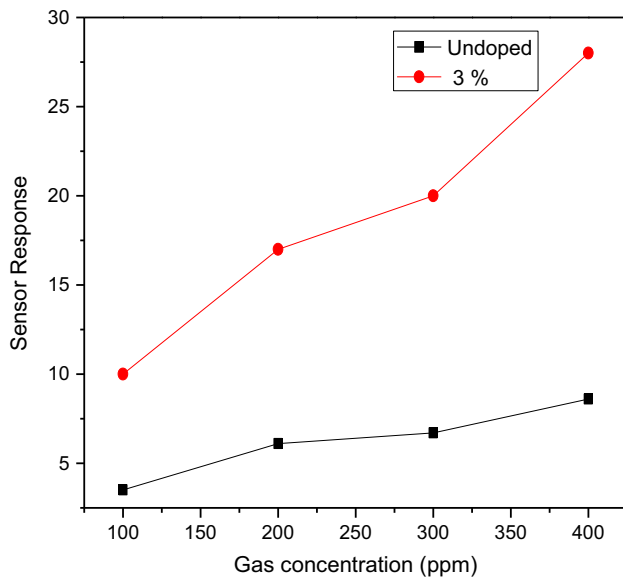
Fig. 13 Variation of sensor response as a function of hydrogen gas concentration

4.4 Variation of sensor response as a function of gas concentration

Figure 13 shows the sensor response of undoped and 3 % doped SnO_2 towards different concentration (100–400 ppm) of hydrogen gas. It is clear from the figure that sensor response increased with increase in hydrogen gas concentration.

5 Conclusions

Undoped and Eu-doped SnO_2 nanoparticles were successfully synthesized by chemical co-precipitation method. Both the undoped as well as Eu-doped samples displayed tetragonal rutile structure. The crystallite size was decreased with increase in dopant concentration. The compressive strain has been increased with increase in dopant concentration. The shifting and broadening of Raman bands is attributed to phonon confinement effect. The contribution of Raman surface modes has been increased with increase in dopant concentration. Decrease in the intensity of emission peaks with increase in dopant concentration ascribed to concentration quenching effect. The enhanced sensing response of doped nanoparticles is attributed to increased surface area of doped nanoparticles. Eu doping has exceptionally increased hydrogen selectivity of synthesized sensor.

References

1. K. Anand, O. Singh, M.P. Singh, J. Kaur, R.C. Singh, Sens. Actuators, B **195**, 409 (2014)
2. A. Azam, A.S. Ahmed, M. Chaman, A.H. Naqvi, J. Appl. Phys. **108**, 094329 (2010)
3. E. Ramasamy, J. Lee, J. Phys. Chem. C **114**, 22032 (2010)
4. J. Lin, Z. Peng, C. Xiang, G. Ruan, Z. Yan, D. Natelson, J.M. Tour, ACS Nano **7**, 6001 (2013)
5. S. Yu, L. Li, D. Xu, H. Dong, Y. Jin, Thin Solid Films **562**, 501 (2014)
6. X. Ding, D. Zeng, C. Xie, Sens. Actuators, B **149**, 336 (2010)
7. Y. Chen, L. Yu, D. Feng, M. Zhuo, M. Zhang, E. Zhang, Z. Xu, Q. Li, T. Wang, Sens. Actuators, B **166–167**, 61 (2012)
8. P. Song, Q. Wang, Z. Yang, Sens. Actuators, B **173**, 839 (2012)
9. N.M. Shaalan, T. Yamazaki, T. Kikuta, Sens. Actuators, B **153**, 11 (2011)
10. G.J. Li, X.H. Zhang, S. Kawi, Sens. Actuators, B **60**, 64 (1999)
11. L. Xiao, S. Shu, S. Liu, Sens. Actuators, B **221**, 120 (2015)
12. J. Wu, Q. Huang, D. Zeng, S. Zhang, L. Yang, D. Xia, Z. Xiong, C. Xie, Sens. Actuators, B **198**, 62 (2014)
13. C. Xu, J. Tamaki, N. Miura, N. Yamazoe, Sens. Actuators, B **3**, 147 (1991)
14. T. Kida, S. Fujiyama, K. Suematsu, M. Yuasa, K. Shimanoe, J. Phys. Chem. C **117**, 17574 (2013)
15. G. Singh, R. Thangaraj, R.C. Singh, Ceram. Int. **42**, 4323 (2016)
16. S. Singh, A. Singh, B.C. Yadav, P.K. Dwivedi, Sens. Actuators, B **177**, 730 (2013)
17. Y. Shen, T. Yamazaki, Z. Liu, D. Meng, T. Kikuta, N. Nakatani, M. Saito, M. Mori, Sens. Actuators, B **135**, 524 (2009)
18. W. Zeng, T. Liu, D. Liu, E. Han, Sens. Actuators, B **160**, 455 (2011)
19. Y. Shen, T. Yamazaki, Z. Liu, D. Meng, T. Kikuta, J. Alloys Compd. **488**, L21 (2009)
20. A.L. Patterson, Phys. Rev. **56**, 978 (1939)
21. B. Venugopal, B. Nandan, A. Ayyachamy, V. Balaji, S. Amirthapandian, B.K. Panigrahi, T. Paramasivam, RSC Adv. **4**, 6141 (2014)
22. B. Nandan, B. Venugopal, S. Amirthapandian, B.K. Panigrahi, P. Thangadurai, J. Nanopart Res. **15**, 1999 (2013)
23. A. Dieguez, A.R. Rodriguez, A. Vila, J.R. Morante, J. Appl. Phys. **90**, 1550 (2001)
24. P. Sangeetha, V. Sasirekha, V. Ramakrishnan, J. Raman Spectrosc. **42**, 1634 (2011)
25. F.H. Aragon, J.A.H. Coaquira, P. Hidalgo, S.W. da Silva, S.L.M. Brito, D. Gouvea, P.C. Morais, J. Raman Spectrosc. **42**, 1081 (2011)
26. J.P. Singh, R.C. Srivastava, H.M. Agrawal, R. Kumar, J. Raman Spectrosc. **42**, 1510 (2011)
27. A.K. Arora, M. Rajalakshmi, T.R. Ravindran, V. Sivasubramanian, J. Raman Spectrosc. **38**, 604 (2007)
28. L.P. Ravaro, L.V.A. Scalvi, A.S. Tabata, F.M.L. Pontes, J.B.B. Oliveira, J. Appl. Phys. **114**, 084304 (2013)
29. S. Loridant, J. Phys. Chem. B **106**, 13273 (2002)
30. R.K. Mishra, A. Kushwaha, P.P. Sahay, RSC Adv. **4**, 3904 (2014)
31. R.K. Mishra, S.K. Pandey, P.P. Sahay, Mater. Res. Bull. **48**, 4196 (2013)
32. P. Sun, X. Zhou, C. Wang, B. Wang, X. Xu, G. Lu, Sens. Actuators **190**, 32 (2014)
33. M.N. Rumyantseva, A.M. Gaskov, N. Rosman, T. Pagnier, J.R. Morante, Chem. Mater. **17**, 893 (2005)